Hydrogen Solubility in FeSi Alloy Phases at High Pressures and Temperatures

Suyu Fu[1,*], Stella Chariton[2], Vitali B. Prakapenka[2], Andrew Chizmeshya[3], Sang-Heon Shim[1,*]

[1] School of Earth and Space Exploration, Arizona State University, Tempe, Arizona, USA.

[2] Center for Advanced Radiation Sources, University of Chicago, Chicago, Illinois, USA.

[3] School of Molecular Sciences, Arizona State University, Tempe, Arizona, USA.

[*] Corresponding authors: suyufu@asu.edu, sshim5@asu.edu

ABSTRACT

Light elements alloying with metallic Fe can change the properties and therefore play a key role in the structure and dynamics of planetary cores. Hydrogen and silicon are possible light elements in the rocky planets' cores. However, hydrogen storage in Fe-Si alloy systems remains unclear at high pressures and high temperatures because of experimental difficulties. Taking advantage of pulsed laser heating combined with high-energy synchrotron X-ray diffraction, we studied reactions between FeSi and H in laser-heated diamond anvil cells up to 61.9 GPa and 3500 K. We found that under H-saturated conditions the amount of H alloying with FeSi (0.3 and <0.1 wt% for the B20 and B2 structures, respectively) is much smaller than that in pure Fe metal (>1.8 wt%). Our experiments also suggest that H remains in the crystal structure of FeSi alloy when recovered to 1 bar. Further density functional theory calculations indicate that the low H solubility likely results from the highly-distorted interstitial sites in the B20 and B2 structures which are not favorable for H incorporation. The recovery of H in the B20 FeSi crystal structure at ambient conditions could open up possibilities to understand geochemical behaviors of H during core formation in future experiments. The low H content in FeSi alloys suggest that if a planetary core is Si rich, Si can limit the ingassing of H into the Fe-rich core.

Key words: FeSi alloy; hydrogen content; planetary cores; pulsed-laser heating; synchrotron X-ray diffraction.

INTRODUCTION

In recent decades, finding habitable planets has drawn interest from not only astrobiologists and astrophysicists but also Earth scientists. Studies indicate that in addition to atmosphere and surface conditions, the interior of a planet could play a key role for its habitability (Shahar et al., 2019). For instance, the dynamo generated by the core would affect the habitability of the surface environment. Light elements are believed to partition

into the Fe metal core during the early magma ocean stage of planets (Stevenson, 2003) and can greatly affect the properties, such as phase relation and melting behavior (Hirose et al., 2013). Considering the diverse sizes and the masses of planets found in the solar system and the exo-planetary systems (Batalha et al., 2011; Jontof-Hutter et al., 2015), from Mars-size rocky planets to gas giants, it is key to studying Fe with light elements for a wide range of pressures.

Hydrogen is the most abundant element in the universe (Anders and Grevesse, 1989; Grevesse and Sauval, 1998). A large amount of H, more than 1.8 wt%, can be dissolved into solid Fe metal at high pressures (Badding et al., 1991; Pépin et al., 2017). Sakamaki et al. (2009) showed that alloying with H can lower the melting temperature of Fe by as much as 600–900 K below 20 GPa. In some models, Si is thought to be the most abundant light element in the Earth's core, up to 12 wt% (Li and Fei, 2003; Hirose et al., 2013). Based on the S/Si ratio and the FeO content of Mercury's surface, its core could contain more than 12 wt% Si (Nittler et al., 2011; Knibbe and van Westrenen, 2018). Therefore, it is important to include Si in Fe metal for understanding the impact of H on the constituent phases of the planetary cores.

Studies on the H content in the Fe–Si system are limited to low pressures and/or low temperatures. Tagawa et al. (2016) conducted laser heating on $Fe_{0.88}Si_{0.12}$ (6.5 wt% Si) in a H medium at 27 and 62 GPa using diamond-anvil cells (DACs), and found that about 1.2–1.5 wt% H can be incorporated into the hexagonal-close-packed (hcp) alloy. However, the heating was conducted below ∼1000 K. For planetary implications, it is important to achieve sufficiently high temperatures over 2000 K. A multi-anvil experiment reported a much lower H solubility of 0.2–0.3 wt% in the B20-structured FeSi alloys up to 20 GPa and 2000 K (Terasaki et al., 2011). However, the pressure range is not sufficiently high for rocky planets' cores greater than that of Mars.

Despite the importance, studying H in laser-heated diamond-anvil cells (LHDACs) has been difficult, because of its fast diffusion into diamond anvils, which can make them brittle. The embrittlement problem becomes more severe with heating, so most studies so far involving H were conducted at temperatures lower than 1500 K (Tagawa et al., 2016; Pépin et al., 2014). Recently, pulsed laser heating combined with gated synchrotron X-ray diffraction (XRD) enabled heating of H to thousands of kelvins in LHDACs (Goncharov et al., 2010). By taking advantage of the development, we have studied reactions between H and FeSi alloy phases in a H-saturated condition up to 61.9 GPa and 3500 K. We have also conducted density functional theory (DFT) calculation to understand the H incorporation mechanism in the FeSi phases and the impact of H on the seismic properties of the Fe-Si alloy phases. Our study on the H content in FeSi provides essential data for understanding the Si-rich cores of some rocky planets. The data can also serve as a benchmark for future studies on H solubility in low-Si Fe-Si alloys.

EXPERIMENTAL METHODS

FeSi powders was purchased from Goodfellow Corporation. Symmetric DACs with culet sizes of 150–300 μm beveled and 200 μm flat were used. Re gaskets were pre-indented and holes with diameters of 2/3 of the culet sizes were drilled as sample chambers. Prepared

gaskets were coated with gold (>80 Å thick) to prevent diffusion of H into Re gaskets forming Re hydrides at high *P-T*. The coating prevents gasket embrittlement by H, which can fail the experiment. The sample was cold pressed into 5–10 μm thick foils using a pair of 400 μm culet diamonds, and then was loaded into the prepared sample chambers. The malleable alloy foil becomes thinner with compression in DAC, likely less than 5 μm. Small pieces of the same starting materials were placed on both sides of the foil to avoid direct contacts between the sample foil and diamond anvils and therefore provide better thermal insulation and laser coupling during heating (Figure 1a). A piece of gold was placed close to the foil, as a pressure calibrant (Ye et al., 2018). This pressure scale (Ye et al., 2018), was compared and shown to be consistent with other commonly used pressure calibrants, such as MgO, Pt, and B2 NaCl. Pressures and their uncertainties were determined by measuring the unit-cell volume of Au before and after each high *P-T* experiment. Pure hydrogen gas was loaded into the DACs as a pressure medium and H source using a gas loading system at Arizona State University. A small ruby chip was put at the edge of the sample chamber to monitor its pressure during gas loading (Figure 1).

Laser heating on the high-pressure samples was conducted at 13-IDD beamline of GeoSoilEnviroCARS (GSECARS) of the Advanced Photon Source (APS), Argonne National Laboratory (ANL). The pulsed laser heating system at the beamline is equipped with a 1064-nm wavelength infrared laser with a flat-top spot size of around 10 μm in diameter (Goncharov et al., 2010). We accumulated 100,000 laser pulses of 1 μs width at a rate of 10 kHz, which totals to 10 s accumulation time (including time between pulses) with a $\sim$0.1-s high-temperature period for each shot. At least ten shots were repeated to allow for a total heating duration of more than 1 s. Considering that H can easily diffuse into metals, $\sim 10^3$ $\mu m^2/s$ even at low *P-T* (Zhang et al., 2008) and the grain size of FeSi powder is $\leq$1 μm, our experimental setup provides sufficient conditions for the sample to fully react with H and possibly to reach the maximum H content. We note that recent experiments used the exact same setups and observed extensive reactions of Fe-S alloys with H (Piet et al., 2021). This shows the effectiveness of the pulsed laser heating to drive chemical reactions between metal alloys and H medium.

Double-sided pulsed laser-heating was conducted on the sample in DACs. Temperatures of both sides were calculated by fitting collected thermal radiation spectra between 670 to 840 nm to a Plank function based on a gray-body approximation. Decompression XRD patterns were collected from 46.1 and 61.9 GPa in two runs. To ensure the reaction between the sample and H, we examined the optical changes in the heated area and conducted 2D XRD and chemical mappings (Figures 1-3). XRD measurements were performed using an incident X-ray beam with a wavelength of 0.3344 Å. We used the PeakPo software for peak identifications and unit-cell fittings (Shim, 2017). The recovered samples were analysed for chemical compositions and mappings using an Electron Probe Micro Analyzer at the Eyring Materials Center of Arizona State University. A JEOL JXA-8530F electron microprobe operated at an accelerating voltage of 15 V and a beam current of 20 nA.

DENSITY FUNCTIONAL THEORY CALCULATIONS

We conducted complementary DFT calculations using the projector augmented-wave (PAW) method with the GPAW package (Blöchl, 1994; Mortensen et al., 2005). The approach combined pseudo-potentials, a plane wave description and all-electron calculations in the frozen core approximation to generate smooth valence wave functions (Mortensen et al., 2005). Both the Perdew-Burke-Ernzerhof (PBE) version of generalized gradient approximation (GGA) (Perdew et al., 1996) and Ceperley-Alder (CA) version of local-density approximation (LDA) (Ceperley and Alder, 1980) were used to carry out simulations on each phase. Convergence tests were conducted for proper plane-wave kinetic energy cutoff and Monkhorst-Pack k-point grid density (Table S1). Convergence was achieved when the maximum total force on all individual atoms falls below 0.005 or 0.01 eV/Å, which allows for optimization of cell shape and internal atomic positions. Static compression equations of state (EoS) were calculated up to 200 GPa with a 10 GPa interval. The pressure-volume data were fit to the 3rd order Birch-Murnaghan (BM) EoS to obtain bulk modulus and its derivative (Table S2). We conducted several test runs on H-free FeSi to compare with literature DFT calculations (Caracas and Wentzcovitch, 2004; Zhao et al., 2011; Vocadlo et al., 1999; Moroni et al., 1999). Our GGA results on the unit-cell volumes of both B20 and B2 FeSi are consistent with the literature (Figure S1 and Table S2) (Caracas and Wentzcovitch, 2004; Zhao et al., 2011). Our LDA predicts slightly higher unit-cell volumes for B2 FeSi than LDA results by Caracas and Wentzcovitch (2004), but comparable to the calculation by Moroni et al. (1999). Considering the overall consistency of the GGA calculation with our experimental data on FeSi alloy phases (Fischer et al., 2014; Sata et al., 2010; Lin et al., 2003), we will mainly discuss the GGA results.

RESULTS AND DISCUSSION

The FeSi alloy has the B20 structure at ambient conditions (Al-Sharif et al., 2001). XRD patterns show that the B20 structure starts to convert to a B20 + B2 mixture with heating in H at ∼20 GPa and ∼2400 K (Figure 4). The coexistence of B20 and B2 was also found in H-free FeSi below 42 GPa (Fischer et al., 2013), which could satisfy the Gibbs phase rule (Smith, 1950). In a H medium, the B20 + B2 mixture completely transforms into pure B2 when heated to 1600–2100 K at 53.0 GPa.

We carefully controlled several important experimental parameters to ensure sufficient reactions between FeSi alloys and H at high P-T. Changes from smooth Debye rings to spotty rings in 2D images and sharpening of the diffraction lines in 1D patterns confirm sufficient heating of the sample (Figures 4 and S2). The line positions shift to lower diffraction angles during laser heating. Such peak shifts remain after temperature quenched to 300 K, indicating the unit-cell volume change and possible incorporation of H into the structure (Figure S3). We repeated heating shots (>10) until the unit-cell volume of the synthesized products did not change after heating so that the H content possibly reaches the maximum at the given P-T. After heating, we conducted 2D XRD mapping, which shows a small difference (0.4%) in the unit-cell volumes of the synthesized products across the heated area (Figure 2). Chemical maps from EPMA of the recovered samples show that Fe:Si ratio did not change in the heated region (Figure 3). These indicate the reaction products between

FeSi alloys and H should be homogeneous without additional phases.

High-quality XRD patterns of the unheated and the heated samples at high pressure and room temperature allow us to obtain preciexse lattice parameters of the B20 and B2 phases (Figures 5 and S3; Table 1). The unit-cell volumes of the unheated region are consistent with those reported for H-free B20 FeSi up to 73 GPa within uncertainties (Fischer et al., 2014; Lin et al., 2003), indicating that the FeSi might not react with H at room temperature (solid black circles in Figure 5). From the agreement, we can also infer a small pressure gradient (<1 GPa) in the sample chamber, likely owing to the compressible H medium. The observed behavior of FeSi is different from pure metallic Fe, which can react with H to form dhcp FeH with expanded volumes even without heating at 300 K (Badding et al., 1991).

With heating up to 2500 K at 20 GPa (Figure 5a-b), the B20 phase shows a <1% greater volume than H-free B20 FeSi. The volume expansion increases up to 4–5% (0.4 Å^3/Atoms) upon more heating runs at 30.1, 42.6, and 46.1 GPa. We note that these unit-cell volumes were collected after heating at 300 K, and H medium provides low deviatoric stress. Therefore, thermal pressure or pressure gradient cannot explain the observed volume expansion in the synthesized phases.

One of the most notable observations is that the unit-cell volume of B20 FeSiH$_x$ remains expanded even after pressure quenching to 1 bar with a lattice parameter of $a = 4.5234(4)$ Å (Figure 4b) compared to $a = 4.4881(5)$ Å for the unheated sample (Table 1). This observation suggests that H remains in the crystal structure of the B20 phase, which is in contrast with the case of pure Fe metal where the high-pressure dhcp FeH phase converts back to a H-free body-centered cubic (bcc) Fe phase upon decompression to 1 bar (Okuchi, 1997; Badding et al., 1991). We note that at 1 bar the unit-cell volume of the unheated sample is consistent with that of H-free B20 FeSi reported in the literature (Fischer et al., 2014), supporting minimal residual pressure. We also observed optical interference fringes between diamond anvil surface and gasket surface, suggesting a gap which vented H medium and released pressure to 1 bar.

Studies have shown that when H is incorporated into pure Fe metal, H would prefer to occupy the octahedral (and possibly tetrahedral) interstitial sites in the face-centered cubic (fcc) or hcp crystal structures to form FeH$_x$ with expanded volumes (Badding et al., 1991; Kato et al., 2020). Accordingly, H contents in the alloys could be estimated empirically using: $x = (V_{\mathrm{MHx}} - V_{\mathrm{M}})/\Delta V_{\mathrm{H}}$, where ΔV_{H}, V_{MHx}, and V_{M} are the volume increase per H atom, and the volumes of metal hydride and H-free metal, respectively (Fukai, 1992). Our observed volume expansion in the B20 phase is much smaller than FeH$_x$ alloys (Figure 6) (Badding et al., 1991; Kato et al., 2020). The ΔV_{H} value is not known for B20 FeSi. If we use an average value of ∼2.5 Å^3/Atoms from literature constraints on transition metals and alloys (Fukai, 1992; Machida et al., 2014; Terasaki et al., 2011), the maximum x in our B20 FeSiH$_x$ is approximately 0.17. This value is comparable to that reported in B20 FeSiH$_x$ synthesized in multi-anvil experiments at low pressures (< 20 GPa), where x is estimated to be 0.07–0.22 (Terasaki et al., 2011). However, the FeSi alloys do not have the close-packed structure, and thus the volume expansion by H in FeSi may be different from those in the close-packed FeH$_x$ phases. We then conducted DFT calculations to gain further insights on the H incorporation mechanism in FeSi alloys as well as its effect on the physical properties.

For a B20 crystal structure, an interstitial site exists at the cubic center which can be occupied by a H atom (Figure 5e). This interstitial site is surrounded by 4Fe and 4Si atoms

(forming tetrahedra independently) with an 8-fold coordination. From the ratio between the interstitial sites and metal atoms (Fe and Si), x in B20 $FeSiH_x$ can range between 0 and 1. We conducted DFT calculations on B20 FeSiH and B20 $FeSiH_{0.25}$, where all and a quarter of the cubic-center interstitial sites in a unit cell are occupied, respectively (Figures 5e and S4a). We found the best match between DFT results on the cubic B20 $FeSiH_{0.25}$ and our experimentally measured unit-cell volumes (Figure 5a-b). The H content is also comparable to our empirical estimations. It should be noted that our DFT calculation was conducted in the static lattice approximation, while the unit-cell volume was measured at 300 K in experiments. We then compared the value of $V(FeSiH_{0.25}) - V(FeSi)$ between experiments and DFT (Figure 5b). This approach reduces (or cancels out) the thermal effect, assuming that the thermal behavior of B20 $FeSiH_{0.25}$ is similar to that of B20 FeSi. Also, there are other factors to be considered, such as limitations of DFT calculations and experimental uncertainties.

In contrast to the case of the B20 phase, below 46.1 GPa the B2 phase synthesized under H-saturated conditions shows unit-cell volumes consistent with those of the H-free B2 FeSi (Fischer et al., 2014; Sata et al., 2010). After the complete transformation from the B20 + B2 mixture into the B2 phase above 53.0 GPa, we noticed a slight volume decrease for the B2 phase, less than 0.2 $Å^3$/Atoms with respect to the H-free case (Figure 5c-d). The volume decrease is 1–2%, greater than the estimated uncertainties. The unit-cell volume decrease caused by H incorporation in B2 FeSi is unusual, because H in the interstitial sites of densely-packed metal alloys typically results in a volume increase (Badding et al., 1991; Kato et al., 2020).

In our DFT calculations, we first attempted interstitial site substitutions at the face centers of a B2 unit cell (Figure S4b). The site has a distorted octahedral shape. For B2 FeSiH, we found 0.6–0.8% unit-cell volume increase, which does not explain our experimental observations (Figure 5c). We, then, hypothesize that H atoms replace equal number of both Fe and Si atoms in the B2 structure (Figure 5f). In order to maintain the size of the cell within computational reasonable level, we conducted DFT calculations on two configurations: B2-structured Fe_7Si_8H and Fe_8Si_7H for $Fe_{15}Si_{15}H_2$. DFT calculations show that both Fe_7Si_8H and Fe_8Si_7H configurations decrease the unit-cell volume from that of H-free B2 FeSi to a similar level of our experimental observations (Figure 5c-d). We also found that the energy difference between Fe_7Si_8H and Fe_8Si_7H configurations is small. If unequal numbers of Fe and Si atoms were replaced, some extra Fe metal or Si phases should have existed. However, none of these phases was observed in our XRD and chemical mappings (Figures 2 and 3), which provide supports for the assumption of replacement of equal Fe and Si. We note that although such a mechanism of H replacing Fe/Si in B2 FeSi can well explain our experimental observations, we do not necessarily rule out other possibilities. For instance, Fukai et al. (2001, 2003) proposed that the Fe-H alloys can form superabundant vacancies under high P-T conditions, which could also cause a volume change.

In a H-free system, Fischer et al. (2014) documented a boundary between the B20 + B2 mixture and B2 structure at ∼42 GPa. With H, our results show that the stability of the H-alloyed B20 FeSi phase extends at least up to 46.1 GPa and 3500 K (Figure 6). That is, adding H into the FeSi alloy shifts the boundary to a higher pressure (46.1–53 GPa). The pressure comparison is likely robust as the Au pressure calibrant in this study is consistent with that of KBr used by Fischer et al. (2014). The expanded stability of B20 relative to

B2 is consistent with the fact that B20 can store more H than B2 as found in this study. We note that the estimated H contents in FeSi alloys are for the quenched solid phases after full reaction with H close to or above melting. Temperature could further change the H solubility in FeSi alloy phases (Tagawa et al., 2021; Okuchi, 1997).

IMPLICATIONS

Our findings of a low H content in solid FeSi alloy phases make an important contrast with Fe metal where high H solubility has been found (Badding et al., 1991), and thus, can affect our understandings on the structure and the dynamics of the planetary cores. Many experiments have been performed to understand H partitioning between silicate melt and Fe metal liquid (Okuchi, 1997; Clesi et al., 2018; Tagawa et al., 2021). However, the H partitioning behavior remains controversial among different studies (Okuchi, 1997; Clesi et al., 2018; Tagawa et al., 2021), likely because of impacts from different experimental methods and H sources. In addition, because H can escape from the high-pressure FeH_x phases during decompression to ambient conditions where bcc Fe metal is stable (Okuchi, 1997; Badding et al., 1991), literature results may be biased if the quantification of H in the metal was performed on the recovered samples (Okuchi, 1997; Clesi et al., 2018; Tagawa et al., 2021). We found that the unit-cell volume of synthesized B20 $FeSiH_x$ remains expanded even at 1 bar. Therefore, H likely remains in the crystal structure of the recovered FeSi sample. This stabilizing effect of Si for H can open up a possibility for accurate measurements of H partitioned into Fe-Si alloys using mass spectrometry.

Tagawa et al. (2021) recently reported that 0.3–0.6 wt% H could partition into liquid Fe alloys while the metal melt coexists with silicate melt at the early Earth's magma ocean. Some of our heating were performed to temperatures above the melting of FeSi and the pressure range overlaps with the conditions expected in the deep magma ocean (Figure 6). Even for those data points with full reaction with H, we found low H solubility in the temperature-quenched solid FeSi alloy (less than 0.3 wt%). Although some H could escape from FeSi during crystallization, we predict that the Si content in Fe alloy liquid of an early magma ocean could limit the amount of H entering into the core.

The effect of H on the elastic properties of Fe-Si alloys can further help us decipher the abundance of light elements in the planetary cores in the solar system and the exo-planetary systems. Here, we calculated the density and the bulk sound speed (V_Φ) of H-bearing B20 and B2 phases and compare them with those of Fe metal and $Fe_{0.88}Si_{0.12}$ alloys (6.5 wt% Si) using literature data (Figure 7) (Dewaele et al., 2006; Pépin et al., 2014; Tagawa et al., 2016; Fischer et al., 2014). Note that these experimental results on Fe, FeH, $Fe_{0.88}Si_{0.12}$, and $Fe_{0.88}Si_{0.12}H_x$ are all documented for 300 K while our DFT results are calculated at essentially 0 K. The temperature impact could be reduced by calculating variations from the respective H-free cases (Figure 7c-d). In this case, we assume that the effect of light elements on the thermal properties of Fe alloys is small. We make a comparison for H/(Fe+Si) = 0.05 in these alloys (∼0.1 wt% H), assuming a linear dependence of these properties with respect to the H content. We found that H decreases density and increases V_Φ for the Fe alloys considered. For both density and V_Φ, the magnitudes of H effect are distinct for B2 compared with B20 FeSi, hcp-$Fe_{0.88}Si_{0.12}$, and hcp-Fe metal (Dewaele et al., 2006; Pépin et al., 2014; Tagawa et al.,

2016; Fischer et al., 2014). We note that H is incorporated into interstitial sites for hcp Fe, hcp $Fe_{0.88}Si_{0.12}$, and B20 FeSi. Here, we attribute the distinct impact of H on density and V_Φ of B2 FeSi to the atomic-scale incorporation mechanism of H as discussed early.

Finally, in this study we demonstrated that heating of planetary materials to very high temperature in a pure H medium became feasible using pulsed laser heating in DAC. Many data points in this study were obtained for heating over 2000 K, which is about 300–1000 K higher than the reported melting of FeH (Sakamaki et al., 2009). The highest temperature at 42.6–46.1 GPa is 3500 K, which is above the melting of FeSi (Figure 6) (Fischer et al., 2014), allowing full reaction between FeSi and H. Although detection of diffuse scattering remains difficult in XRD when combined with pulsed laser heating, it is feasible that the *P-T* conditions expected for the outer core can be achieved for H-bearing Fe alloys in the future studies using similar experimental configurations.

ACKNOWLEDGEMENTS

The authors thank A. Wittmann for his assistance on electron microprobe analyses of the recovered samples. This work is supported by NSF-Astronomical Science (AST200567) and NSF-Earth Science (EAR1921298). We acknowledge the support of GeoSoilEnviroCARS (University of Chicago, Sector 13) for synchrotron experiments. GeoSoilEnviroCARS was supported by the National Science Foundation - Earth Sciences (EAR-1634415). This research used resources of the Advanced Photon Source, a U.S. Department of Energy (DOE) Office of Science User Facility operated for the DOE Office of Science by Argonne National Laboratory under Contract No. DE-AC02-06CH11357.

References

Al-Sharif, A., Abu-Jafar, M., and Qteish, A. Structural and electronic structure properties of FeSi: the driving force behind the stability of the B20 phase. *Journal of Physics: Condensed Matter*, 13(12):2807, 2001.

Anders, E. and Grevesse, N. Abundances of the elements: Meteoritic and solar. *Geochimica et Cosmochimica acta*, 53(1):197–214, 1989.

Badding, J., Hemley, R., and Mao, H. High-pressure chemistry of hydrogen in metals: In situ study of iron hydride. *Science*, 253(5018):421–424, 1991.

Batalha, N. M., Borucki, W. J., Bryson, S. T., Buchhave, L. A., Caldwell, D. A., Christensen-Dalsgaard, J., Ciardi, D., Dunham, E. W., Fressin, F., Gautier III, T. N., et al. Kepler's first rocky planet: -10b. *The Astrophysical Journal*, 729(1):27, 2011.

Blöchl, P. E. Projector augmented-wave method. *Physical review B*, 50(24):17953, 1994.

Caracas, R. and Wentzcovitch, R. Equation of state and elasticity of fesi. *Geophysical Research Letters*, 31(20), 2004.

Ceperley, D. M. and Alder, B. J. Ground state of the electron gas by a stochastic method. *Physical review letters*, 45(7):566, 1980.

Clesi, V., Bouhifd, M. A., Bolfan-Casanova, N., Manthilake, G., Schiavi, F., Raepsaet, C., Bureau, H., Khodja, H., and Andrault, D. Low hydrogen contents in the cores of terrestrial planets. *Science advances*, 4(3):e1701876, 2018.

Dewaele, A., Loubeyre, P., Occelli, F., Mezouar, M., Dorogokupets, P. I., and Torrent, M. Quasihydrostatic equation of state of iron above 2 Mbar. *Physical Review Letters*, 97(21): 215504, 2006.

Fischer, R. A., Campbell, A. J., Reaman, D. M., Miller, N. A., Heinz, D. L., Dera, P., and Prakapenka, V. B. Phase relations in the Fe–FeSi system at high pressures and temperatures. *Earth and Planetary Science Letters*, 373:54–64, 2013.

Fischer, R. A., Campbell, A. J., Caracas, R., Reaman, D. M., Heinz, D. L., Dera, P., and Prakapenka, V. B. Equations of state in the Fe-FeSi system at high pressures and temperatures. *Journal of Geophysical Research: Solid Earth*, 119(4):2810–2827, 2014.

Fukai, Y. Some properties of the Fe-H system at high pressures and temperatures, and their implications for the Earth's core. *High Pressure Research: Application to Earth and Planetary Sciences*, pages 373–385, 1992.

Fukai, Y., Haraguchi, T., Hayashi, E., Ishii, Y., Kurokawa, Y., and Yanagawa, J. Hydrogen-induced superabundant vacancies and diffusion enhancement in some fcc metals. In *Defect and Diffusion Forum*, volume 194, pages 1063–1068. Trans Tech Publ, 2001.

Fukai, Y., Mori, K., and Shinomiya, H. The phase diagram and superabundant vacancy formation in fe–h alloys under high hydrogen pressures. *Journal of alloys and compounds*, 348(1-2):105–109, 2003.

Goncharov, A. F., Prakapenka, V. B., Struzhkin, V. V., Kantor, I., Rivers, M. L., and Dalton, D. A. X-ray diffraction in the pulsed laser heated diamond anvil cell. *Review of Scientific Instruments*, 81(11):113902, 2010.

Grevesse, N. and Sauval, A. Standard solar composition. *Space Science Reviews*, 85(1): 161–174, 1998.

Hirose, K., Labrosse, S., and Hernlund, J. Composition and state of the core. *Annual Review of Earth and Planetary Sciences*, 41:657–691, 2013.

Jontof-Hutter, D., Rowe, J. F., Lissauer, J. J., Fabrycky, D. C., and Ford, E. B. The mass of the mars-sized exoplanet -138 b from transit timing. *Nature*, 522(7556):321–323, 2015.

Kato, C., Umemoto, K., Ohta, K., Tagawa, S., Hirose, K., and Ohishi, Y. Stability of fcc phase FeH to 137 GPa. *American Mineralogist: Journal of Earth and Planetary Materials*, 105(6):917–921, 2020.

Knibbe, J. S. and van Westrenen, W. The thermal evolution of mercury's fe–si core. *Earth and Planetary Science Letters*, 482:147–159, 2018.

Li, J. and Fei, Y. Experimental constraints on core composition. *Treatise on geochemistry*, 2:568, 2003.

Lin, J.-F., Campbell, A. J., Heinz, D. L., and Shen, G. Static compression of iron-silicon alloys: Implications for silicon in the Earth's core. *Journal of Geophysical Research: Solid Earth*, 108(B1), 2003.

Machida, A., Saitoh, H., Sugimoto, H., Hattori, T., Sano-Furukawa, A., Endo, N., Katayama, Y., Iizuka, R., Sato, T., Matsuo, M., et al. Site occupancy of interstitial deuterium atoms in face-centred cubic iron. *Nature communications*, 5(1):1–6, 2014.

Moroni, E., Wolf, W., Hafner, J., and Podloucky, R. Cohesive, structural, and electronic properties of Fe-Si compounds. *Physical Review B*, 59(20):12860, 1999.

Mortensen, J. J., Hansen, L. B., and Jacobsen, K. W. Real-space grid implementation of the projector augmented wave method. *Physical Review B*, 71(3):035109, 2005.

Nittler, L. R., Starr, R. D., Weider, S. Z., McCoy, T. J., Boynton, W. V., Ebel, D. S., Ernst, C. M., Evans, L. G., Goldsten, J. O., Hamara, D. K., et al. The major-element composition of mercury's surface from messenger x-ray spectrometry. *Science*, 333(6051): 1847–1850, 2011.

Okuchi, T. Hydrogen partitioning into molten iron at high pressure: implications for Earth's core. *Science*, 278(5344):1781–1784, 1997.

Pépin, C. M., Dewaele, A., Geneste, G., Loubeyre, P., and Mezouar, M. New iron hydrides under high pressure. *Physical review letters*, 113(26):265504, 2014.

Pépin, C. M., Geneste, G., Dewaele, A., Mezouar, M., and Loubeyre, P. Synthesis of FeH5: A layered structure with atomic hydrogen slabs. *Science*, 357(6349):382–385, 2017.

Perdew, J. P., Burke, K., and Ernzerhof, M. Generalized gradient approximation made simple. *Physical review letters*, 77(18):3865, 1996.

Piet, H., Leinenweber, K., Greenberg, E., Prakapenka, V. B., and Shim, S.-H. Effects of hydrogen on the phase relations in Fe–FeS at pressures of Mars-sized bodies. *Journal of Geophysical Research: Planets*, page e2021JE006942, 2021.

Sakamaki, K., Takahashi, E., Nakajima, Y., Nishihara, Y., Funakoshi, K., Suzuki, T., and Fukai, Y. Melting phase relation of FeH_x up to 20 GPa: Implication for the temperature of the Earth's core. *Physics of the Earth and Planetary Interiors*, 174(1-4):192–201, 2009.

Sata, N., Hirose, K., Shen, G., Nakajima, Y., Ohishi, Y., and Hirao, N. Compression of FeSi, Fe_3C, $Fe_{0.95}O$, and FeS under the core pressures and implication for light element in the Earth's core. *Journal of Geophysical Research: Solid Earth*, 115(B9), 2010.

Shahar, A., Driscoll, P., Weinberger, A., and Cody, G. What makes a planet habitable? *Science*, 364(6439):434–435, 2019.

Shim, S. PeakPo - a python software for x-ray diffraction analysis at high pressure and high temperature. *Zenodo: Meyrin, Switzerland*, 2017.

Smith, J. M. Introduction to chemical engineering thermodynamics, 1950.

Stevenson, D. J. Planetary magnetic fields. *Earth and planetary science letters*, 208(1-2): 1–11, 2003.

Tagawa, S., Ohta, K., Hirose, K., Kato, C., and Ohishi, Y. Compression of Fe–Si–H alloys to core pressures. *Geophysical Research Letters*, 43(8):3686–3692, 2016.

Tagawa, S., Sakamoto, N., Hirose, K., Yokoo, S., Hernlund, J., Ohishi, Y., and Yurimoto, H. Experimental evidence for hydrogen incorporation into earth's core. *Nature communications*, 12(1):1–8, 2021.

Terasaki, H., Shibazaki, Y., Sakamaki, T., Tateyama, R., Ohtani, E., Funakoshi, K.-i., and Higo, Y. Hydrogenation of fesi under high pressure. *American Mineralogist*, 96(1):93–99, 2011.

Vocadlo, L., Price, G. D., and Wood, I. Crystal structure, compressibility and possible phase transitions in ϵ-FeSi studied by first-principles pseudopotential calculations. *Acta Crystallographica Section B: Structural Science*, 55(4):484–493, 1999.

Ye, Y., Shim, S.-H., Prakapenka, V., and Meng, Y. Equation of state of solid ne inter-calibrated with the mgo, au, pt, nacl-b2, and ruby pressure scales up to 130 gpa. *High Pressure Research*, 38(4):377–395, 2018.

Zhang, G., Yukawa, H., Watanabe, N., Saito, Y., Fukaya, H., Morinaga, M., Nambu, T., and Matsumoto, Y. Analysis of hydrogen diffusion coefficient during hydrogen permeation through pure niobium. *International journal of hydrogen energy*, 33(16):4419–4423, 2008.

Zhao, K., Jiang, G., and Wang, L. Electronic and thermodynamic properties of B2-FeSi from first principles. *Physica B: Condensed Matter*, 406(3):363–367, 2011.

Table 1: Unit-cell parameters of the B20 and B2 phases synthesized in a H medium at high pressures. These data points were measured during compression or decompression at 300 K. The synthesis P-T conditions are given in the first raw of each subsection. Uncertainties on the last digit(s) are shown in parentheses.

Pressure (GPa)	a(Au) (Å)	a(B20) (Å)	a(B2) (Å)	Pressure (GPa)	a(Au) (Å)	a(B20) (Å)	a(B2) (Å)
Unheated (fresh) region, Cold compression				42.6 GPa and 1446-3820 K, Compression			
ambient	-	4.4881(7)	-	42.6(15)	3.8659(10)	4.3200(9)	2.6479(2)
21.4(7)	3.9478(5)	4.3402(6)	-	45.5(12)	3.8564(9)	4.2953(11)	2.6430(2)
31.1(7)	3.9074(5)	4.3002(7)	-	45.8(17)	3.8554(11)	4.2957(12)	2.6422(2)
36.0(9)	3.8891(7)	4.2799(7)	-	46.1 GPa and 1900-3500 K, Decompression			
42.6(9)	3.8659(7)	4.2536(9)	-	46.1(18)	3.8545(12)	4.2977(10)	2.6415(4)
48.1(15)	3.8482(11)	4.2326(10)	-	45.2(30)	3.8573(16)	4.2983(16)	2.6419(4)
50.2(10)	3.8417(8)	4.2122(10)	-	43.6(11)	3.8625(8)	4.3062(18)	2.6453(5)
55.3(9)	3.8268(7)	4.2028(10)	-	38.9(21)	3.8785(12)	4.3227(20)	2.6545(4)
55.4(9)	3.8265(7)	4.2059(10)	-	33.5(26)	3.8982(14)	4.3336(22)	2.6641(3)
57.7(11)	3.8200(9)	4.1935(13)	-	33.7(24)	3.8974(13)	4.3393(30)	2.6640(7)
58.3(18)	3.8183(12)	4.1895(15)	-	31.4(22)	3.9063(12)	4.3499(10)	2.6682(3)
61.8(22)	3.8089(14)	4.1808(14)	-	17.4(8)	3.9684(5)	4.4058(8)	2.7049(3)
63.0(22)	3.8057(13)	4.1755(16)	-	13.1(3)	3.9912(2)	4.4460(7)	2.7284(2)
67.5(20)	3.7941(12)	4.1616(16)	-	8.9(3)	4.0158(2)	4.4724(6)	2.7468(2)
73.5(25)	3.7795(14)	4.1524(22)	-	ambient	-	4.5234(3)	2.7772(2)
21.4 GPa and 1830-2485 K, Compression				53.3 GPa and 1670-2100 K, Compression			
21.4(3)	3.9478(3)	4.3577(4)	-	53.0(10)	3.8334(8)	-	2.6147(4)
26.0(5)	3.9284(4)	4.3400(4)	-	57.5(13)	3.8206(10)	-	2.6071(5)
27.7(6)	3.9212(4)	4.3338(5)	-	57.8(13)	3.8197(10)	-	2.6054(5)
29.1(8)	3.9154(7)	4.3291(6)	-	61.9 GPa and 1700-2160 K, Decompression			
30.1(9)	3.9114(8)	4.3245(6)	-	61.9(14)	3.8086(10)	-	2.5980(6)
30.7(11)	3.9090(9)	4.3227(7)	-	61.9(14)	3.8086(10)	-	2.5964(6)
31.1 GPa and 1409-2650 K, Compression				62.3(15)	3.8075(12)	-	2.5950(7)
31.1(11)	3.9074(8)	4.3312(5)	2.6751(1)	58.3(20)	3.8183(13)	-	2.6015(7)
32.1(14)	3.9035(11)	4.3264(6)	2.6721(1)	58.9(22)	3.8167(13)	-	2.6020(6)
33.9(15)	3.8967(12)	4.3206(6)	2.6688(1)	57.7(26)	3.8200(14)	-	2.6035(6)
35.3(20)	3.8914(14)	4.3154(6)	2.6658(2)	55.4(11)	3.8265(9)	-	2.6060(4)
38.0(22)	3.8817(14)	4.3062(6)	2.6594(2)	48.2(13)	3.8479(10)	-	2.6276(4)
39.7(26)	3.8757(16)	4.2977(7)	2.6555(2)	27.6(15)	3.9216(11)	-	2.6911(3)
41.8(11)	3.8685(8)	4.2896(7)	2.6516(2)	0.3(12)	4.0763(9)	-	2.7750(2)
42.6(13)	3.8659(10)	4.2845(7)	2.6511(2)	ambient	-	-	2.7758(2)

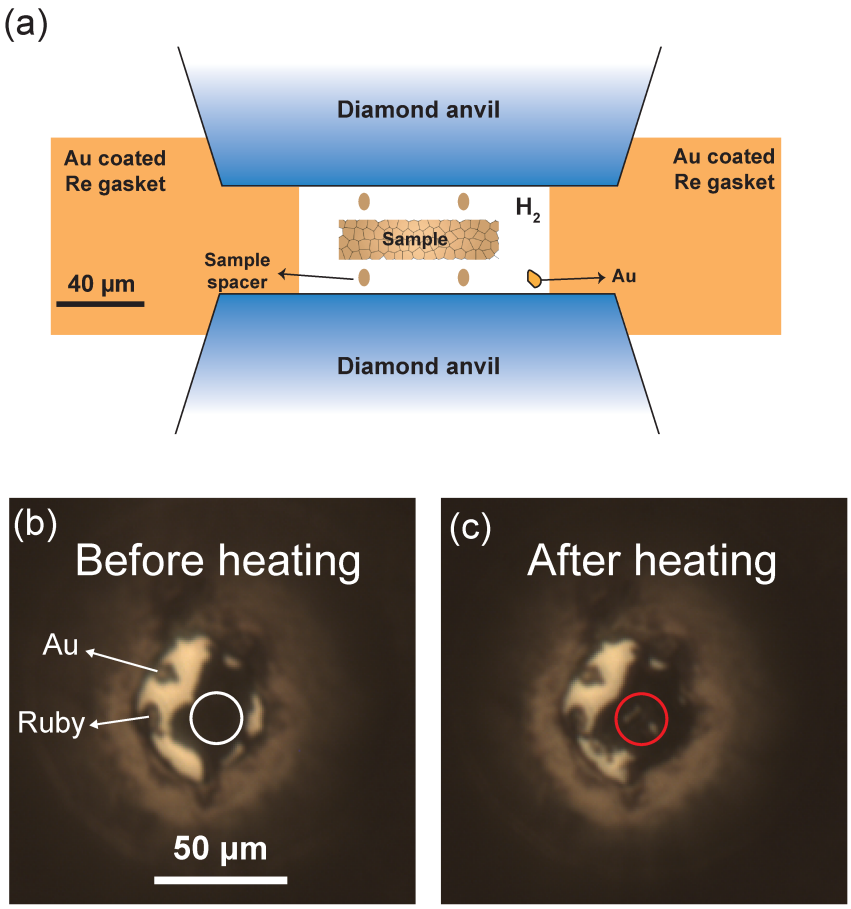

Figure 1: Laser heating of FeSi in a hydrogen medium at high P-T. (a) A schematic diagram of a DAC loaded with a FeSi sample foil in a hydrogen medium. The foil was made by cold compressing FeSi powder (an average grain size of $\sim$1 μm) to an initial thickness of 5–10 μm. The hydrogen gas likely penetrates into the sample foil and exists around the grain boundaries. (b) and (c) Images of the sample in a diamond-anvil cell at 61.9 GPa and 300 K taken before and after laser heating up to 2200 K, respectively. The circles highlight the heated area. The white spots in (b) are from migration of some metal samples by melting at high temperatures.

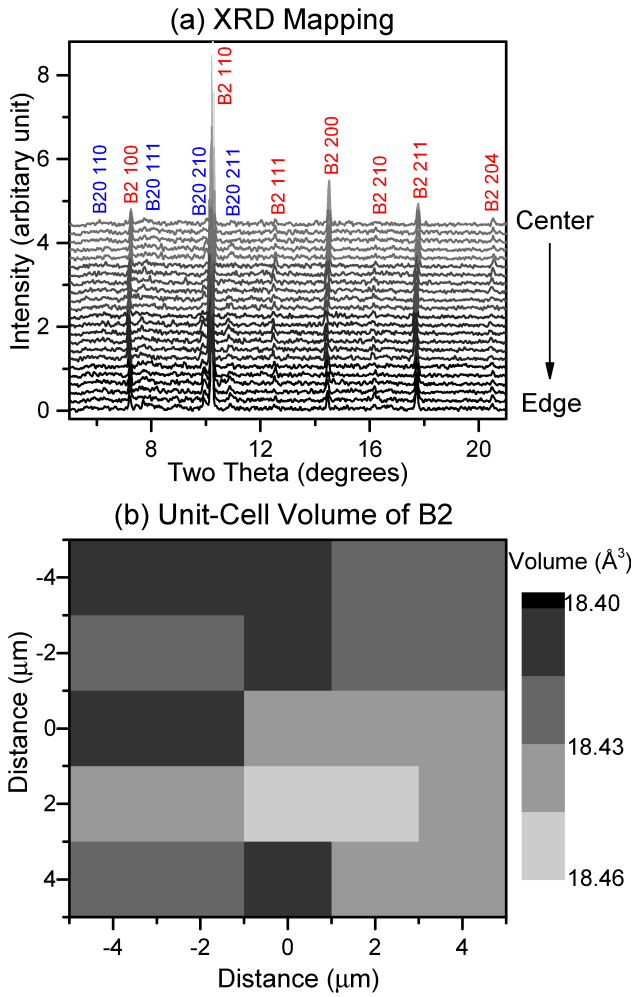

Figure 2: Two dimensional XRD mapping of the heated region at 46.1 GPa and 300 K. (a) XRD patterns measured after heating up to 3500 K at 46.1 GPa. The patterns from top to bottom were collected from the heated center to the edge of the hot spot within an 8×8 μm^2 area with a 2 μm step. The B2 structure is dominant with some weak peaks from B20. The Miller indices of the B20 and B2 phases are presented in the blue and red labels, respectively. No additional peaks were found in any of the heated area, suggesting no new phases other than B2 and B20 exist after laser heating at high pressure. The wavelength of the incident X-ray is 0.3344 Å. (b) A 2D map of the unit-cell volumes of the synthesized B2 phase at 46.1 GPa and 300 K. A small volume difference (0.4%) indicates that the synthesized products are homogeneous over the heated region.

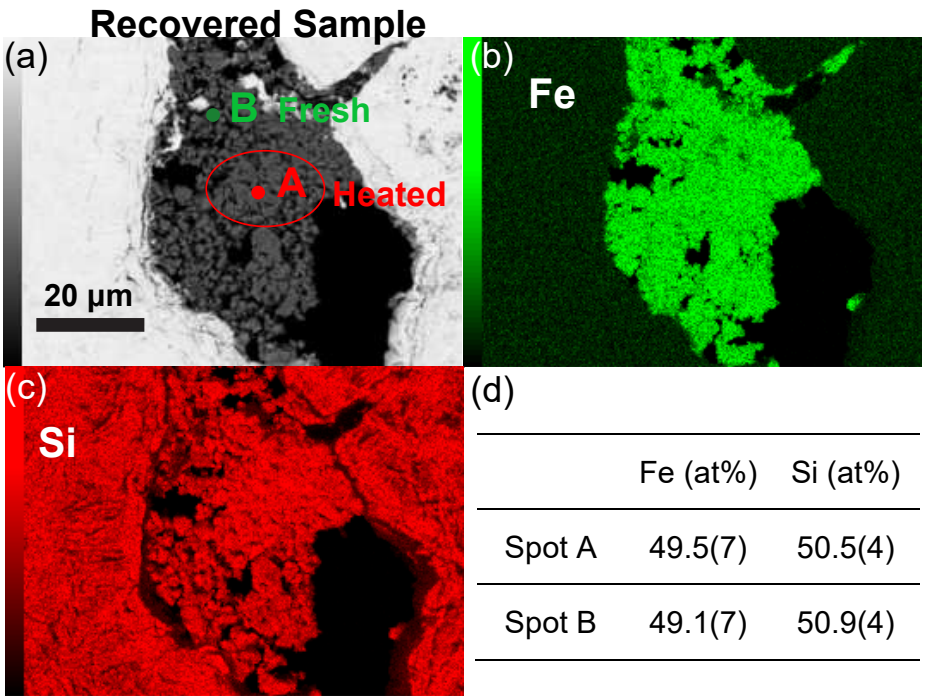

	Fe (at%)	Si (at%)
Spot A	49.5(7)	50.5(4)
Spot B	49.1(7)	50.9(4)

Figure 3: Electron probe micro analyzer measurements on the recovered FeSi sample from 61.9 GPa and 2200 K. (a) A back-scattered electron image. Spots A and B are heated and unheated areas, respectively. (b) and (c) Energy-dispersive spectroscopy maps of Fe and Si, respectively. (d) Quantitative measurements for the chemical compositions of spots A and B in (a). We found little changes in the Fe and Si contents of the sample after heating. The changed unit-cell volumes of B20 and B2 in the heated spot detected from XRD (refer to Figures 4-5) provide strong evidence on the incorporation of H into the crystal structure of FeSi.

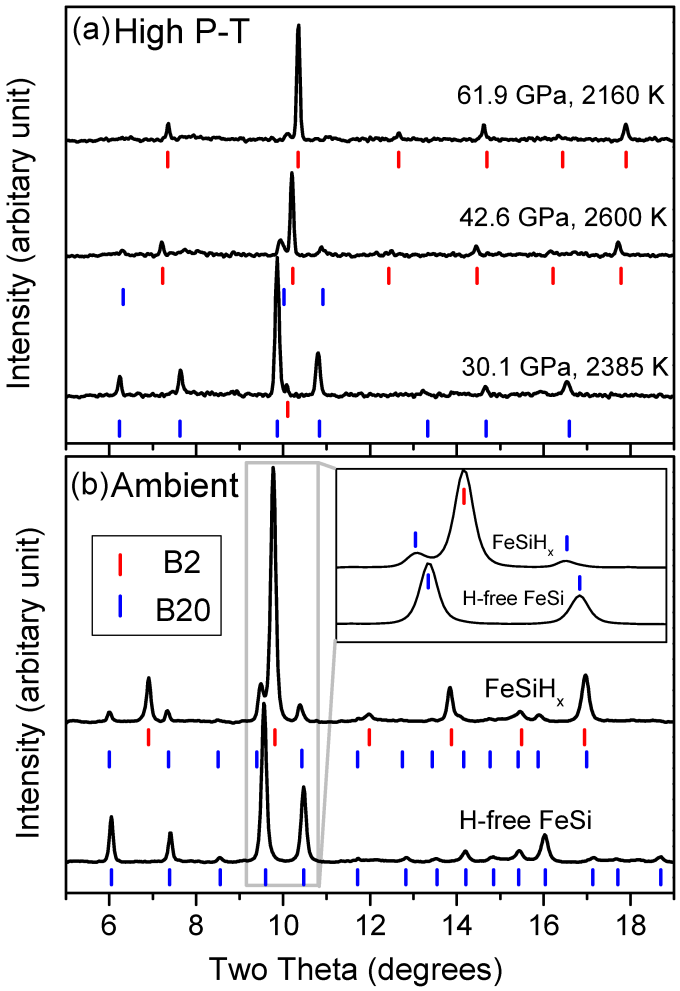

Figure 4: (a) X-ray diffraction patterns at *in situ* high P-T. At 30.1 GPa and 2385 K, B20 is the main phase (the blue ticks) and a weak peak of the B2 (the red ticks) phase appear. With a pressure increase to 42.6 GPa, heating up to 2600 K results in a conversion to the B2 structure, which coexists with the weak B20 structure. At 61.9 GPa and 2160 K, the B20 structure completely transforms into the B2 structure. (b) Diffraction patterns of the recovered $FeSiH_x$ at ambient conditions, compared with H-free FeSi. $FeSiH_x$ shows larger d-spacings than the H-free FeSi alloys as highlighted in the inset which is a zoom-in view of the gray rectangular area. The wavelength of incident X-ray is 0.3344 Å.

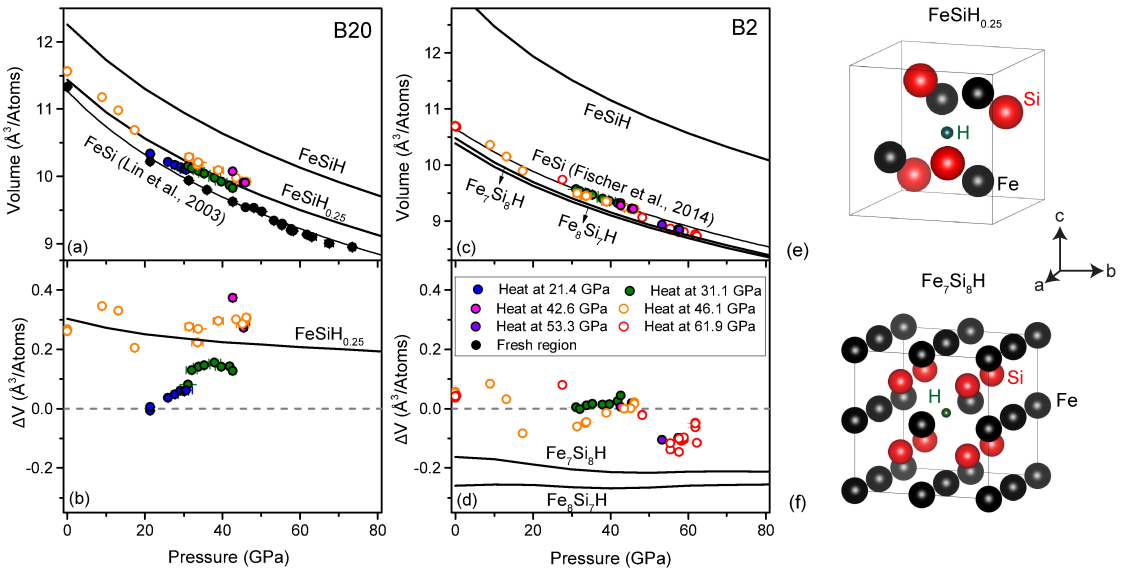

Figure 5: The volumes of the synthesized (a and b) B20 and (c and d) B2 $FeSiH_x$ phases. The volumes per atoms are shown in (a) and (c), and the volume changes (ΔV) due to H incorporation are shown in (b) and (d). ΔV is the difference between the measured volumes of H-bearing $FeSiH_x$ and H-free FeSi (Fischer et al., 2014; Lin et al., 2003). The legend in (d) is shared for (a)-(d), showing different heating conditions in this study. The open and solid symbols are decompression and compression data, respectively. The thin black curves are for H-free FeSi (Lin et al., 2003; Fischer et al., 2014). The thick curves are for the DFT-GGA calculations for H-bearing $FeSiH_x$ alloy phases with the labeled compositions. We show crystal structure models for the H alloying with (e) B20 and (f) B2 FeSi. For B20, H occupies the interstitial sites at the cubic center to form $FeSiH_{0.25}$, where only a quarter of the sites in a unit cell are occupied. For the slight volume decrease found in B2, instead of interstitial sites, H may replace one Fe and one Si atoms to form $Fe_{15}Si_{15}H_2$. The substitution mechanism was modeled with two separate configurations of 2×2×2 cells of Fe_7Si_8H and Fe_8Si_7H. The estimated uncertainties for pressures and volumes are shown but they are in general smaller than the size of symbols.

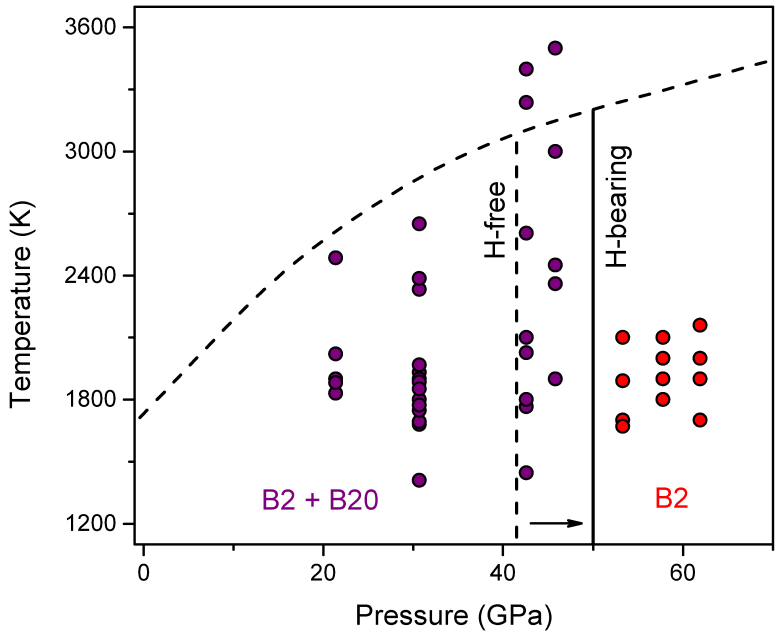

Figure 6: Observations of stable $FeSiH_x$ phases at high P-T. The solid purple and red circles represent coexistence of B2 and B20 phases and pure B2 phase, respectively. The solid black line indicates the estimated phase boundary of synthesized H-bearing $FeSiH_x$ alloys. The dashed black lines are the melting curve and the phase boundary of stoichiometric FeSi (Fischer et al., 2014).

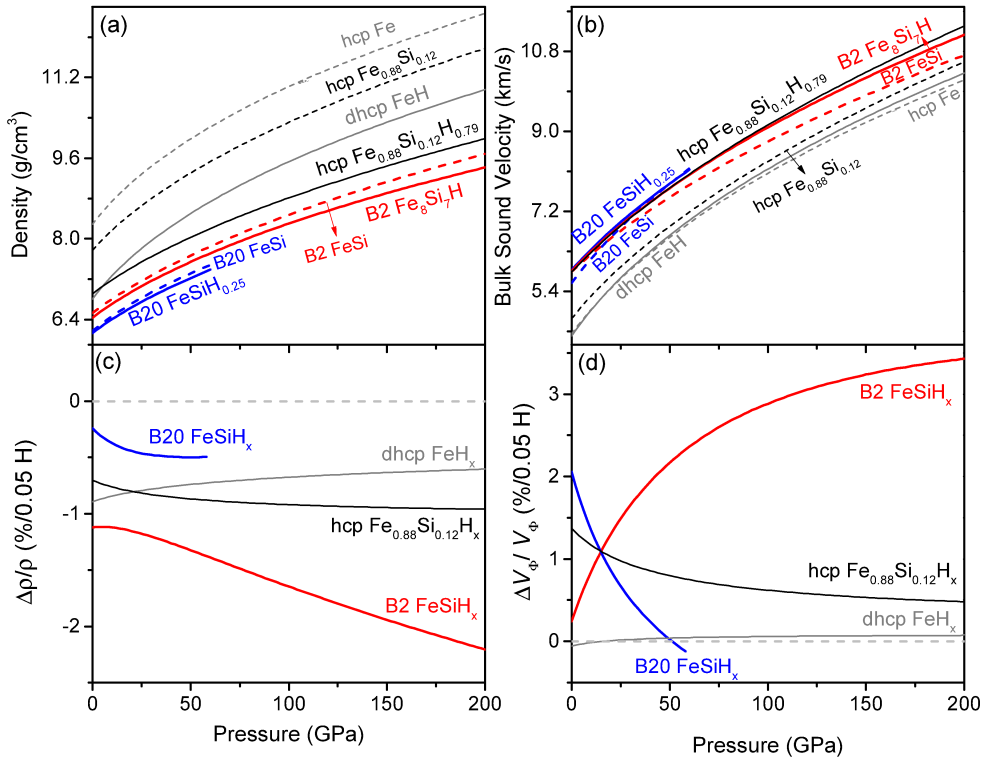

Figure 7: Modeled (a and c) density and (b and d) bulk sound velocity of H-bearing (solid curves) and H-free (dashed curves) FeSi alloys at high pressures and essentailly 0 K. (c) and (d) Variations of density and bulk sound velocity of $FeSiH_x$ phases by $x = 0.1$ or H/(Fe+Si) = 0.05 compared to H-free cases. Properties of B20 and B2 phases are obtained from our GGA calculations. We compare these results with hcp Fe (Dewaele et al., 2006), dhcp FeH (Pépin et al., 2014), hcp $Fe_{0.88}Si_{0.12}$ and hcp $Fe_{0.88}Si_{0.12}H_{0.79}$ (Tagawa et al., 2016).